

Non-separable frequency dependence of two-particle vertex in interacting fermion systems

D. Vilardi, C. Taranto, and W. Metzner

Max Planck Institute for Solid State Research, Heisenbergstrasse 1, D-70569 Stuttgart, Germany

(Dated: August 10, 2017)

We derive functional flow equations for the two-particle vertex and the self-energy in interacting fermion systems which capture the full frequency dependence of both quantities. The equations are applied to the hole-doped two-dimensional Hubbard model as a prototype system with entangled magnetic, charge and pairing fluctuations. Each fluctuation channel acquires substantial dependences on all three Matsubara frequencies, such that the frequency dependence of the vertex cannot be accurately represented by a channel sum with only one frequency variable in each term. At the temperatures we are able to access, the leading instabilities are mostly antiferromagnetic, with an incommensurate wave vector. However, at large doping, a divergence in the charge channel occurs at a finite frequency transfer, if the vertex flow is computed without self-energy feedback. This enigmatic instability was already observed in a calculation by Husemann *et al.* [Phys. Rev. B, **85**, 075121 (2012)], who used an approximate separable ansatz for the frequency dependence of the vertex. We identify a simple mechanism for this instability in terms of a random phase approximation for the charge channel with a frequency dependent effective magnetic interaction as input. The frequency dependent self-energy is generically affected only mildly by the strongly momentum and frequency dependent two-particle vertex. At the moderate interaction strength where our approach is applicable, we obtain a moderate reduction of the quasi-particle weight and a sizable decay rate with a pronounced momentum dependence. Nevertheless, the self-energy feedback into the vertex flow turns out to be crucial, as it suppresses the unphysical finite frequency charge instability.

I. INTRODUCTION

Exact flow equations describing the evolution of correlation functions upon a successive scale-by-scale evaluation of functional integrals have become a powerful source of new approximation methods in statistical field theory¹ and in the theory of quantum many-body systems – especially interacting Fermi systems.² Among the various versions of these Wilsonian flows, which go under the name *functional renormalization group* (fRG), Wetterich's³ flow equation for the generating functional of one-particle irreducible vertex functions turned out to be particularly efficient. While (approximate) non-perturbative solutions of the flow equations are possible for interacting bosons, for fermions one has to rely on an expansion in the fields, truncating the exact hierarchy of flow equations beyond m -particle vertex functions of a certain order. One may, however, expand around a non-perturbative starting point, such as the dynamical mean-field solution.⁴

The two-particle vertex is a key quantity in any fermionic fRG flow, as it determines the two-particle correlations, leading instabilities, and also the flow of the self-energy. Unfortunately, in quantum systems the two-particle vertex is a difficult object to deal with, due to its dependence on three momentum and frequency arguments. In weakly interacting Fermi systems one may discard the frequency dependence and the momentum dependence perpendicular to the Fermi surface, as these are irrelevant in power counting. This simplification was the basis for early fRG studies of the two-dimensional Hubbard model, using an approximate static parametrization of the vertex, with a momentum dependence discretized

by partitioning the Brillouin zone in patches.^{5–8} Later alternative treatments of the momentum dependence using expansions with form factors were devised.^{9–11}

While irrelevant in power counting, the frequency dependence of the vertex becomes important upon approaching instabilities toward symmetry breaking in the flow.¹² Even for weak bare interactions the two-particle vertex becomes large in that regime and acquires singular frequency dependences, for example those associated with the Goldstone boson.¹⁰ The frequency dependence plays an increasingly important role at strong coupling, as has been confirmed for impurity models,^{13,14} and in the dynamical mean field theory (DMFT).^{15,16} Hence, a proper treatment of the frequency dependence of the vertex is mandatory for methods dealing with the interplay between fluctuations in all the channels at strong coupling, such as the combination of DMFT and fRG (DMF²RG),⁴ and other non-local diagrammatic extensions of the DMFT.¹⁷

A simplified treatment of the frequency dependence, based on an additive decomposition of the two-particle vertex in pairing, magnetic and charge fluctuation channels, was developed by Husemann *et al.*,¹² and applied to an fRG flow for the two-dimensional Hubbard model. They devised an approximate parametrization, where the dependence of the vertex on the three fermionic frequencies is assumed to be *separable*, that is, each channel depends only on one bosonic transfer frequency, a linear combination of two fermionic frequencies. Already at this level the frequency dependence turned out to be important even at moderate coupling strengths, affecting significantly the energy scale of the leading instabilities. Moreover, for some model parameters an unexpected di-

vergence without any plausible physical interpretation was found in the charge channel at zero momentum and *finite* frequency transfer.¹²

In this paper we present fRG flows for the two-particle vertex without making any simplifying assumptions or approximations on its frequency dependence. The two-dimensional Hubbard model is used as a prototype fermion system featuring strong and competing fluctuations in several channels. We demonstrate the feasibility, and in some respects, also the necessity of a computation with an unbiased frequency parametrization, even at moderate coupling. Significant *non-separable* frequency dependences appear. The various interaction channels do not depend on the bosonic transfer frequencies only, but also on the remaining two fermionic frequencies. We recover the enigmatic charge instability discovered by Husemann et al.,¹² and reveal its mechanism as the impact of a frequency dependent magnetic interaction on the charge channel.

While a static vertex entails a static self-energy in the one-particle irreducible fRG formalism, the implementation of the full dynamics allows us to compute the frequency (and momentum) dependence of the self-energy. Most interestingly, the feedback of the self-energy into the flow equation for the vertex eliminates the unphysical divergence in the charge channel. This is in contrast with the widespread assumption that the self-energy feedback plays a minor role at moderate interaction strengths.

The paper is structured as follows. In Sec. II we will introduce the two-dimensional Hubbard model and the fRG flow equations for the two-particle vertex and the self-energy. After discussing the channel decomposition and our parametrization of the two-particle vertex in Sec. III, we will move on to the discussion of the main results in Sec. IV. Here we identify the leading instabilities, and we discuss the flow of the frequency-dependent vertex. For the charge divergence we provide a transparent explanation, and we finally discuss the momentum and frequency dependence of the self-energy. We draw our conclusions in Sec. V. In the Appendix A we report all the final expression for the vertex flow equations, while in the Appendix B we show the frequency dependence also in the pairing channel.

II. FORMALISM

A. Model

The Hubbard model¹⁸ describes spin- $\frac{1}{2}$ fermions with a local interaction:

$$\mathcal{H} = \sum_{i,j,\sigma} t_{ij} c_{i,\sigma}^\dagger c_{j,\sigma} + U \sum_i n_{i,\uparrow} n_{i,\downarrow}, \quad (1)$$

where $c_{i,\sigma}^\dagger$ ($c_{i,\sigma}$) creates (annihilates) a fermion on site i with spin orientation σ (\uparrow or \downarrow). We consider the two-dimensional case on a square lattice and repulsive interaction $U > 0$ at finite temperature T . The hopping

amplitude is restricted to $t_{ij} = -t$ for nearest neighbors, $t_{ij} = -t'$ for next-to-nearest neighbors. Fourier transforming the hopping matrix yields the bare dispersion relation

$$\varepsilon_{\mathbf{k}} = -2t(\cos k_x + \cos k_y) - 4t' \cos k_x \cos k_y. \quad (2)$$

B. Flow equations

In the following paragraph we will provide some details about the functional renormalization group for interacting fermion systems,^{2,19} defining in particular the notation used for the vertex.

The fRG implements a scale-by-scale evaluation of the functional integral describing the many-body system. This is done by endowing the bare action with an additional dependence on a scale-parameter Λ ,

$$\mathcal{S}^\Lambda[\bar{\psi}, \psi] = -(\bar{\psi}, G_0^{\Lambda^{-1}} \psi) + \mathcal{S}_{\text{int}}, \quad (3)$$

where \mathcal{S}_{int} is the interaction part, and $(\bar{\psi}, \psi)$ denotes the summation over all the quantum numbers of the fermionic fields $\bar{\psi}$ and ψ . The scale dependence, acquired through the non-interacting propagator G_0^Λ , generates flow equations (with known initial conditions) for generating functionals. These are defined via functional integrals with the action \mathcal{S}^Λ . Examples are the generating functional for the connected Green's function and its Legendre transform, the so-called average effective action.³ The final result is recovered for some final Λ -value restoring the original bare propagator, $G_0^{\Lambda_f} = G_0$, so that the physical action of interest is recovered.

We will apply this approach to the effective action, whose expansions in the fields generates the one-particle irreducible (1PI) vertex functions. By expanding the functional flow equation,³ one obtains a hierarchy of flow equations for the 1PI functions, involving vertices of arbitrarily high orders. We will restrict ourselves to the two-particle level truncation by retaining only the two lowest nonvanishing orders in the expansion, that is, we consider the flow of the self-energy Σ^Λ and of the two-particle vertex V^Λ , neglecting the effects of higher order vertices. This truncation restricts the applicability of the approach to the weak-to-moderate coupling regime.²⁰ It can be further shown that, at the two-particle level truncation, the fRG sums up efficiently, although approximately, the so-called parquet-diagrams.²¹

Due to SU(2) symmetry, the self-energy is diagonal in spin-space:

$$\Sigma_{\sigma\sigma'}^\Lambda(k) = \Sigma(k) \delta_{\sigma,\sigma'}, \quad (4)$$

where $k = (\mathbf{k}, \nu)$, ν is a fermionic Matsubara frequency and \mathbf{k} a momentum in the first Brillouin zone.

For the notation of the two-particle vertex function $V_{\sigma_1\sigma_2\sigma_3\sigma_4}(k_1, k_2, k_3)$ we refer to Fig. 1, where $k_i = (\mathbf{k}_i, \nu_i)$. The momentum $k_4 = k_1 + k_2 - k_3$ is fixed by momentum conservation. The SU(2) spin-rotation symmetry guarantees that the vertex vanishes for all the

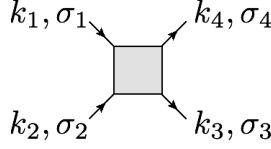


Figure 1. Notation of the two-particle vertex.

six spin combinations apart from six: $V_{\uparrow\uparrow\uparrow\uparrow}^\Lambda = V_{\downarrow\downarrow\downarrow\downarrow}^\Lambda$, $V_{\uparrow\downarrow\uparrow\downarrow}^\Lambda = V_{\downarrow\uparrow\downarrow\uparrow}^\Lambda$, and $V_{\uparrow\downarrow\downarrow\uparrow}^\Lambda = V_{\downarrow\uparrow\uparrow\downarrow}^\Lambda$. Finally, due to SU(2) symmetry and crossing relation one has¹⁶

$$V_{\uparrow\uparrow\uparrow\uparrow}^\Lambda(k_1, k_2, k_3) = V_{\uparrow\downarrow\uparrow\downarrow}^\Lambda(k_1, k_2, k_3) - V_{\uparrow\downarrow\downarrow\uparrow}^\Lambda(k_1, k_2, k_1 + k_2 - k_3), \quad (5)$$

$$V_{\uparrow\downarrow\uparrow\downarrow}^\Lambda(k_1, k_2, k_3) = -V_{\uparrow\downarrow\downarrow\uparrow}^\Lambda(k_1, k_2, k_1 + k_2 - k_3). \quad (6)$$

This allows us to express the vertex by only one function of three frequency-momentum arguments:

The flow equation for the vertex can be written as^{2,9}

$$\frac{d}{d\Lambda} V^\Lambda(k_1, k_2, k_3) = \mathcal{T}_{pp}^\Lambda(k_1, k_2, k_3) + \mathcal{T}_{ph}^\Lambda(k_1, k_2, k_3) + \mathcal{T}_{phc}^\Lambda(k_1, k_2, k_3), \quad (9)$$

where²²

$$\mathcal{T}_{pp}^\Lambda(k_1, k_2, k_3) = -\frac{1}{2} \int_p \mathcal{P}_{pp}^\Lambda(k_1 + k_2, p) \left\{ V^\Lambda(k_1, k_2, k_1 + k_2 - p) V^\Lambda(k_1 + k_2 - p, p, k_3) + V^\Lambda(k_1, k_2, p) V^\Lambda(p, k_1 + k_2 - p, k_3) \right\}, \quad (10)$$

$$\mathcal{T}_{ph}^\Lambda(k_1, k_2, k_3) = - \int_p \mathcal{P}_{ph}^\Lambda(k_3 - k_1, p) \left\{ 2V^\Lambda(k_1, k_3 - k_1 + p, k_3) V^\Lambda(p, k_2, k_3 - k_1 + p) - V^\Lambda(k_1, k_3 - k_1 + p, p) V^\Lambda(p, k_2, k_3 - k_1 + p) - V^\Lambda(k_1, k_3 - k_1 + p, k_3) V^\Lambda(k_2, p, k_3 - k_1 + p) \right\}, \quad (11)$$

$$\mathcal{T}_{phc}^\Lambda(k_1, k_2, k_3) = \int_p \mathcal{P}_{phc}^\Lambda(k_2 - k_3, p) V^\Lambda(k_1, k_2 - k_3 + p, p) V^\Lambda(p, k_2, k_3). \quad (12)$$

Here \mathcal{T}_{pp}^Λ , \mathcal{T}_{ph}^Λ and $\mathcal{T}_{phc}^\Lambda$ stand respectively for *particle-particle*, *particle-hole* and *particle-hole crossed* contributions. We have defined the quantities

$$\mathcal{P}_{ph}^\Lambda(Q, p) = G^\Lambda(Q + p) S^\Lambda(p) + G^\Lambda(p) S^\Lambda(Q + p), \quad (13)$$

$$\mathcal{P}_{pp}^\Lambda(Q, p) = G^\Lambda(Q - p) S^\Lambda(p) + G^\Lambda(p) S^\Lambda(Q - p), \quad (14)$$

which are the scale derivatives, at fixed self-energy, of the product of two Green's functions.

C. Interaction flow

To use the flow equations defined above we need to specify the Λ -dependence of the non-interacting propagator G_0^Λ . We use the *interaction cutoff*, introduced by

$V^\Lambda(k_1, k_2, k_3) \equiv V_{\uparrow\downarrow\uparrow\downarrow}^\Lambda(k_1, k_2, k_3)$ where all the others spin components are obtained by Eqs. (5-6).⁹

The flow equation for the self energy can then be written as²

$$\frac{d}{d\Lambda} \Sigma^\Lambda(k) = - \int_p S^\Lambda(p) [2V^\Lambda(k, p, p) - V^\Lambda(k, p, k)], \quad (7)$$

with $p = (\mathbf{p}, \omega)$ and $k = (\mathbf{k}, \nu)$. We use the notation $\int_p = T \sum_\omega \int_{\mathbf{p}}$, where \sum_ω is the Matsubara frequency sum, and $\int_{\mathbf{p}} = \int \frac{d\mathbf{p}}{(2\pi)^2}$ is the normalized integration over the first Brillouin zone.

$$S^\Lambda = \left. \frac{dG^\Lambda}{d\Lambda} \right|_{\Sigma^\Lambda = \text{const}} \quad (8)$$

is the so-called single-scale propagator, and G^Λ is the full propagator, which is related to the bare propagator and the self-energy by the Dyson equation $(G_0^\Lambda)^{-1} = (G^\Lambda)^{-1} - \Sigma^\Lambda$.

Honerkamp *et al.*:²³

$$G_0^\Lambda(k) = \Lambda G_0(k) = \frac{\Lambda}{i\nu + \mu^\Lambda - \varepsilon_{\mathbf{k}}}, \quad (15)$$

where the scale-parameter Λ flows from 0 to 1. We have introduced a Λ -dependent chemical potential to maintain the density fixed during the flow. The Dyson equation yields the interacting Green's function in the form

$$G^\Lambda(k) = \frac{\Lambda}{i\nu - \varepsilon_{\mathbf{k}} + \mu^\Lambda - \Lambda \Sigma^\Lambda(k)}. \quad (16)$$

The scale-dependent chemical potential μ^Λ is determined from the equation

$$n = n^\Lambda(\mu^\Lambda) \equiv 2 \int_k \frac{e^{i\nu 0^+}}{i\nu - \varepsilon_{\mathbf{k}} + \mu^\Lambda - \Lambda \Sigma^\Lambda(k)}. \quad (17)$$

The factor 2 accounts for the spin degree of freedom.

The main advantage of the interaction cutoff is that the Λ -dependent action can be interpreted²³ as the physical action of the system with a rescaled interaction $U^\Lambda = \Lambda^2 U$. Since T acts as an infrared cutoff, for our purposes we do not need to worry about the fact that this cutoff is not scale-selective, and hence does not regularize possible divergences in the bubbles.

III. VERTEX APPROXIMATION

To parametrize the momentum and frequency dependence of the two-particle vertex, we use the channel decomposition of the vertex introduced by Husemann and Salmhofer,⁹ where the vertex is written as a sum of the bare interaction and fluctuation induced effective pairing, magnetic and charge interactions. The function $V^\Lambda(k_1, k_2, k_3)$ is thus decomposed as

$$\begin{aligned} V^\Lambda(k_1, k_2, k_3) = & U - \phi_p^\Lambda(k_1 + k_2; k_1, k_3) \\ & + \phi_m^\Lambda(k_3 - k_1; k_1, k_2) \\ & + \frac{1}{2}\phi_m^\Lambda(k_2 - k_3; k_1, k_2) \\ & - \frac{1}{2}\phi_c^\Lambda(k_2 - k_3; k_1, k_2), \end{aligned} \quad (18)$$

with the *pairing* channel ϕ_p , the *magnetic* channel ϕ_m and the *charge* channel ϕ_c . The first argument of ϕ_p is the conserved total momentum and frequency of the particles, while the first argument of ϕ_m and ϕ_c is a momentum and frequency transfer. Substituting Eq. (18) into Eq. (9) we obtain:

$$\begin{aligned} & -\dot{\phi}_p^\Lambda(k_1 + k_2; k_1, k_3) + \dot{\phi}_m^\Lambda(k_3 - k_1; k_1, k_2) \\ & + \frac{1}{2}\dot{\phi}_m^\Lambda(k_2 - k_3; k_1, k_2) - \frac{1}{2}\dot{\phi}_c^\Lambda(k_2 - k_3; k_1, k_2) \quad (19) \\ & = \mathcal{T}_{pp}^\Lambda(k_1, k_2, k_3) + \mathcal{T}_{ph}^\Lambda(k_1, k_2, k_3) + \mathcal{T}_{phc}^\Lambda(k_1, k_2, k_3). \end{aligned}$$

We associate the total momentum argument of \mathcal{P}_{pp}^Λ and the momentum transfer argument of \mathcal{P}_{ph}^Λ in Eqs. (10-12) to the corresponding arguments of the ϕ_x on the right hand side of Eq. 18. This way, it is easy to attribute \mathcal{T}_{pp}^Λ to the flow equation of the only function in Eq. (20) that depends explicitly on $k_1 + k_2$: $-\dot{\phi}_p^\Lambda = \mathcal{T}_{pp}^\Lambda$. The same is true for the particle-hole crossed channel: $\mathcal{T}_{phc}^\Lambda = \dot{\phi}_m^\Lambda$. We associate to the particle-hole diagram the third and fourth term on the left hand side of Eq. (20): $\mathcal{T}_{ph}^\Lambda(k_1, k_2, k_3) = \frac{1}{2}\dot{\phi}_m^\Lambda(k_2 - k_3; k_1, k_2) - \frac{1}{2}\dot{\phi}_c^\Lambda(k_2 - k_3; k_1, k_2)$. The flow equations for ϕ_x then read:⁹

$$\dot{\phi}_p^\Lambda(Q; k_1, k_3) = -\mathcal{T}_{pp}^\Lambda(k_1, Q - k_1, k_3), \quad (20)$$

$$\begin{aligned} \dot{\phi}_c^\Lambda(Q; k_1, k_2) = & \mathcal{T}_{phc}^\Lambda(k_1, k_2, Q + k_1) \\ & - 2\mathcal{T}_{ph}^\Lambda(k_1, k_2, k_2 - Q), \end{aligned} \quad (21)$$

$$\dot{\phi}_m^\Lambda(Q; k_1, k_2) = \mathcal{T}_{phc}^\Lambda(k_1, k_2, Q + k_1). \quad (22)$$

Following Refs. 9 and 12, we address first the momentum dependence. To parametrize the dependence on the

fermionic momenta, we use a decomposition of unity by means of a set of orthonormal form factors $\{f_l(\mathbf{k})\}$. We can then project each channel on a subset of form factors, whose choice is physically motivated.⁹

For the pairing channel we keep only $f_s(\mathbf{k}) = 1$ and $f_d(\mathbf{k}) = \cos k_x - \cos k_y$:

$$\begin{aligned} \phi_p^\Lambda(Q; k_1, k_3) = & \mathcal{S}_{\mathbf{Q}, \Omega}^\Lambda(\nu_1, \nu_3) \\ & + f_d\left(\frac{\mathbf{Q}}{2} - \mathbf{k}_1\right) f_d\left(\frac{\mathbf{Q}}{2} - \mathbf{k}_3\right) \mathcal{D}_{\mathbf{Q}, \Omega}^\Lambda(\nu_1, \nu_3). \end{aligned} \quad (23)$$

A divergence in the channel \mathcal{S} (\mathcal{D}) is associated to the emergence of *s*-wave (*d*-wave) superconductivity.^{2,19}

For the charge and magnetic channels we restrict ourselves to $f_s(\mathbf{k}) = 1$ only:

$$\phi_c^\Lambda(Q; k_1, k_2) = \mathcal{C}_{\mathbf{Q}, \Omega}^\Lambda(\nu_1, \nu_2), \quad (24)$$

$$\phi_m^\Lambda(Q; k_1, k_2) = \mathcal{M}_{\mathbf{Q}, \Omega}^\Lambda(\nu_1, \nu_2). \quad (25)$$

A divergence of these functions signals *s*-wave instabilities in the charge and magnetic channels, respectively.

Each channel in Eq. (18) contains a (bosonic) linear combination of momenta and frequencies, and two remaining independent fermionic momentum and frequency variables. The choice of the mixed notation is natural since the bosonic momenta and frequencies play a special role in the diagrammatics. Indeed, it is the only dependence generated in second order perturbation theory and the main dependence in finite order perturbation theory. Although one expects a dominant dependence on the bosonic frequency, in particular in the weak coupling regime, we will see that the dependence on the fermionic frequencies can become strong and not negligible, too. In Refs. 9 and 12, with no or a simplified frequency dependence, the channel functions are interpreted as bosonic exchange propagators. Such an interpretation is not possible with full frequency-dependence.

The flow equations for the channels \mathcal{S} , \mathcal{D} , \mathcal{C} and \mathcal{M} can be derived from the projection of Eqs. (20)-(22) onto the form factors:

$$\dot{\mathcal{S}}_{\mathbf{Q}, \Omega}^\Lambda(\nu_1, \nu_3) = - \int_{\mathbf{k}_1, \mathbf{k}_3} \mathcal{T}_{pp}^\Lambda(k_1, Q - k_1, k_3), \quad (26)$$

$$\begin{aligned} \dot{\mathcal{D}}_{\mathbf{Q}, \Omega}^\Lambda(\nu_1, \nu_3) = & - \int_{\mathbf{k}_1, \mathbf{k}_3} f_d\left(\frac{\mathbf{Q}}{2} - \mathbf{k}_1\right) f_d\left(\frac{\mathbf{Q}}{2} - \mathbf{k}_3\right) \\ & \times \mathcal{T}_{pp}^\Lambda(k_1, Q - k_1, k_3), \end{aligned} \quad (27)$$

$$\begin{aligned} \dot{\mathcal{C}}_{\mathbf{Q}, \Omega}^\Lambda(\nu_1, \nu_2) = & \int_{\mathbf{k}_1, \mathbf{k}_2} \mathcal{T}_{phc}^\Lambda(k_1, k_2, Q + k_1) \\ & - 2\mathcal{T}_{ph}^\Lambda(k_1, k_2, k_2 - Q), \end{aligned} \quad (28)$$

$$\dot{\mathcal{M}}_{\mathbf{Q}, \Omega}^\Lambda(\nu_1, \nu_2) = \int_{\mathbf{k}_1, \mathbf{k}_2} \mathcal{T}_{phc}^\Lambda(k_1, k_2, Q + k_1). \quad (29)$$

The final equations are then obtained by substituting the decomposition (18) into the equations above, and using trigonometric identities.

As an example we report here the equations for the

magnetic channel, while the expressions for the other channels are presented in the Appendix A:

$$\dot{\mathcal{M}}_{\mathbf{Q},\Omega}^{\Lambda}(\nu_1, \nu_2) = \sum_{\nu} L_{\mathbf{Q},\Omega}^{\text{m},\Lambda}(\nu_1, \nu) P_{\mathbf{Q},\Omega}^{\Lambda}(\nu) L_{\mathbf{Q},\Omega}^{\text{m},\Lambda}(\nu, \nu_2 - \Omega), \quad (30)$$

with

$$P_{\mathbf{Q},\Omega}^{\Lambda}(\omega) = \int_{\mathbf{p}} G^{\Lambda}(\mathbf{p}, \omega) S^{\Lambda}(\mathbf{Q} + \mathbf{p}, \Omega + \omega) + G^{\Lambda}(\mathbf{Q} + \mathbf{p}, \Omega + \omega) S^{\Lambda}(\mathbf{p}, \omega), \quad (31)$$

and

$$\begin{aligned} L_{\mathbf{Q},\Omega}^{\text{m},\Lambda}(\nu_1, \nu_2) = & U + \mathcal{M}_{\mathbf{Q},\Omega}^{\Lambda}(\nu_1, \nu_2) + \int_{\mathbf{p}} \left\{ -\mathcal{S}_{\mathbf{p},\nu_1+\nu_2}^{\Lambda}(\nu_1, \nu_1 + \Omega) - \frac{1}{2} \mathcal{D}_{\mathbf{p},\nu_1+\nu_2}^{\Lambda}(\nu_1, \nu_1 + \Omega) [\cos(Q_x) + \cos(Q_y)] \right. \\ & \left. + \frac{1}{2} [\mathcal{M}_{\mathbf{p},\nu_2-\nu_1-\Omega}^{\Lambda}(\nu_1, \nu_2) - \mathcal{C}_{\mathbf{p},\nu_2-\nu_1-\Omega}^{\Lambda}(\nu_1, \nu_2)] \right\} \end{aligned} \quad (32)$$

Note that after the momentum integrals in P and L are performed, the right hand side of Eq. (30) can be expressed as a matrix multiplication in frequency space, where Ω and \mathbf{Q} appear as parameters.

After this decomposition, the evaluation of the vertex-flow equation, depending on six arguments, is reduced to the flow of the four functions \mathcal{S} , \mathcal{D} , \mathcal{C} , \mathcal{M} , each of them depending on three frequencies and one momentum only. In order to compute these equations numerically we discretize the momentum dependence on patches covering the Brillouin zone and truncate the frequency dependence to some maximal frequency value.

IV. RESULTS

In this section we present our results obtained by the full frequency dependent fRG. All the results are presented in units of the nearest-neighbor hopping $t = 1$. Unless specified otherwise, the next-nearest-neighbor hopping is $t' = -0.32t$, the interaction strength $U = 4t$, and the temperature $T = 0.08t$.

We have implemented numerically the flow equations reported in the Appendix. To take into account the distinct momentum dependences of the self-energy and the vertex, we have defined two different patching schemes of the respective Brillouin zones. Similarly to what is done in Ref. 9, the vertex patching describes more accurately the corners around $(0,0)$ and (π,π) , where we expect the instability vectors. For the self-energy, the most relevant physics happens in the vicinity of the Fermi surface. Therefore we concentrate the patches along the Fermi surface and in its immediate vicinity (see Figs. 10(a) and 10(b)), with more points close to the *antinodal* region near $(\pi,0)$, relevant for antiferromagnetism. In the calculations presented in the following we have used 29 patches for the vertex and 44 for the self-energy.

For the implementation of the frequency dependence

we found it convenient to rewrite \mathcal{S} , \mathcal{D} , \mathcal{C} and \mathcal{M} as functions of three bosonic frequencies. For each frequency argument we restricted ourselves to at least 40 positive and 40 negative Matsubara frequencies. Beyond these frequencies we have used the asymptotic values.

A. Analysis of instabilities

By means of the fRG one can perform an instability analysis of the system: for some value of the flow parameter Λ one of the channels shows a divergence. The value Λ_c for which this happens is called *critical scale*, and from the diverging channel one can infer the leading instability of the system. In Fig. 2 we show the critical scale $1 - \Lambda_c$ as a function of the doping $x = 1 - n$ with and without self-energy feedback. For the physical interpretation of Λ_c in the interaction flow, we refer to the rescaled interaction²³ \tilde{U}^{Λ} discussed in Sec. II C.

We defined the critical scale as the flow parameter for which the value of the largest channel exceeds $200t$. We checked that these results are also consistent with a stability analysis based on the susceptibilities.

A divergence of the vertex at finite temperature is associated with spontaneous symmetry breaking, in violation of the Mermin-Wagner theorem.²⁴ This is a consequence of the truncation of the flow equations. Instead, we should interpret the finite temperature vertex divergence as the signal of the appearance of strong bosonic fluctuations that cannot be treated within the approximation-scheme we are using.²⁰ Even though in our framework the flow cannot be continued beyond the critical scale, from the analysis of vertex and self-energy we can identify the relevant effective interactions of the system.

For the parameter sets shown in Fig. 2, and without self-energy feedback, there are two possible instabilities. For doping smaller than 0.35 the leading fluc-

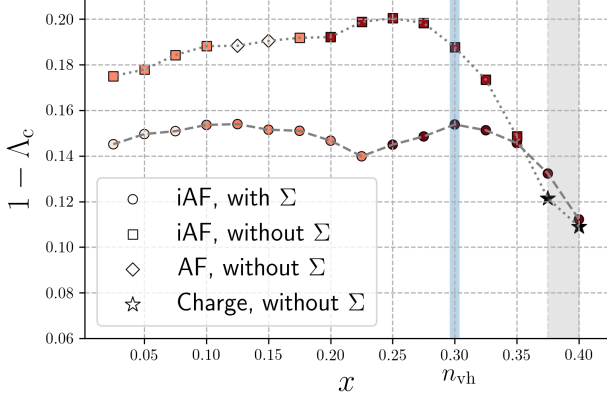


Figure 2. Critical scale $1 - \Lambda_c$ as a function of doping $x = 1 - n$, for $T = 0.08t$, $t' = -0.32t$ and $U = 4t$. Square symbols and circles refer to incommensurate antiferromagnetism (iAF) without and with self-energy feedback, respectively. The black stars refer to a divergence in the charge channel at $\mathbf{Q} = (0, 0)$. The color of squares and circles encodes the distance of the incommensurate magnetic \mathbf{Q} -vector from (π, π) : darker color corresponds to a larger distance. The darkest color corresponds to $\delta = 1.13$. The vertical light blue line marks van Hove filling.

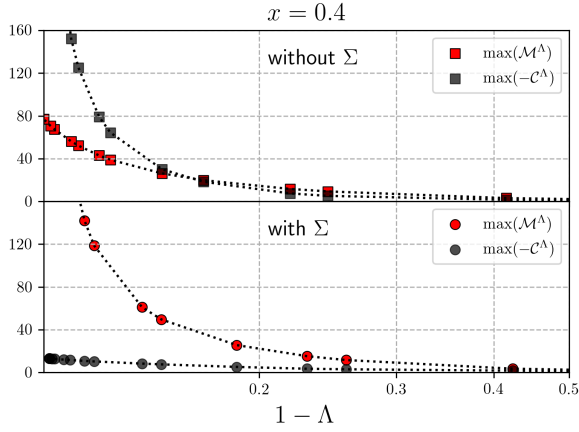


Figure 3. Flow of the maximal values of the charge (\mathcal{C}) and magnetic (\mathcal{M}) channels as functions of $1 - \Lambda$, for $x = 0.4$, $t' = -0.32$, $U = 4t$ and $T = 0.08t$. Top: without self-energy feedback; bottom: with self-energy feedback.

tations of the system are antiferromagnetic, with a commensurate (AF) wave vector $\mathbf{Q} = (\pi, \pi)$, or an incommensurate (iAF) wave vector of the form $\mathbf{Q} = (\pi, \pi - \delta)$. The incommensurability δ is determined by the momentum \mathbf{Q} where the magnetic channel \mathcal{M}^Λ has its maximum. The region of commensurate antiferromagnetism for $0.125 \leq x \leq 0.150$ has to be attributed to the presence of a large plateau around (π, π) in the bare bubble. Correspondingly, the commensurate antiferromagnetic instability is almost degenerate with an incommensurate one.

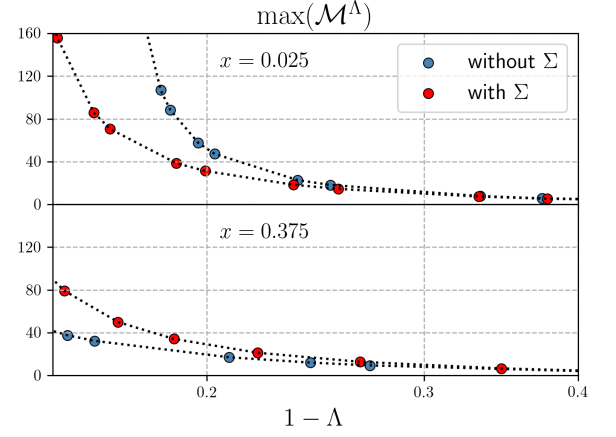


Figure 4. Flow of the maximal values of the magnetic (\mathcal{M}) channel as functions of $1 - \Lambda$, for $x = 0.025$ (top) and $x = 0.375$ (bottom). The other parameters are $t' = -0.32$, $U = 4t$ and $T = 0.08t$. Red symbols: with self-energy feedback; blue symbols: without self-energy feedback.

The most striking feature in Fig. 2 is the presence of a divergence in the charge channel \mathcal{C}^Λ at $\mathbf{Q} = (0, 0)$ for the largest values of doping, marked by black stars. This feature was already observed in a fRG calculation with a simplified frequency parametrization by Husemann *et al.* in Ref. 12 and named *scattering instability*. The charge channel \mathcal{C}^Λ diverges for a non-zero frequency transfer $\Omega = 2\pi T$, which does not allow for a natural interpretation in terms of a physical instability. The frequency structure of the charge channel \mathcal{C}^Λ together with its origin will be discussed further in paragraph IV C.

The self-energy feedback has three effects. First, it decreases $1 - \Lambda_c$. Second, the incommensurability vector is affected, the region of commensurate antiferromagnetism disappears, and one can observe a more regular trend of increasing δ with x . Third, the divergence in the charge channel is completely suppressed, and the leading instability in the doping region $0.375 \leq x \leq 0.4$ remains incommensurate antiferromagnetism. This can be also seen from Fig. 3, where we compare the flow of the maximum (of the absolute value) of magnetic and charge channels with and without the self-energy feedback for doping $x = 0.4$. Without self-energy feedback, the charge channel reaches large and negative values. The presence of such a large (and negative) charge channel inhibits the magnetic channel. The effect of the self-energy in the flow is evident: the charge channel is strongly damped. At the same time the magnetic channel is enhanced.

This is confirmed by Fig. 4, where we show the maximum of \mathcal{M} with and without self-energy feedback for $x = 0.025$ (top) and $x = 0.375$ (bottom). One can see that the enhancement of \mathcal{M} due to the self-energy is specific of the large doping region, while, in the small doping region the self energy decreases \mathcal{M} . The self-energy affects the magnetic channel directly by reducing the particle-hole bubble, and indirectly through the

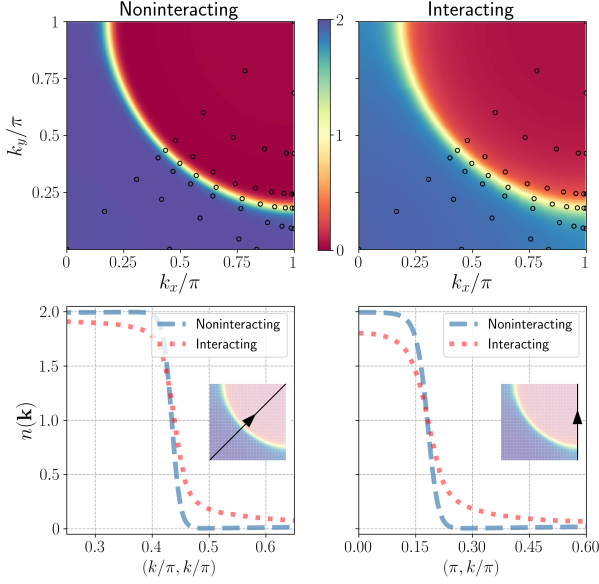


Figure 5. Top row: momentum distribution for $t' = -0.32t$, $T = 0.08t$ and doping $x = 0.025$. Left panel: non-interacting case. Right panel: interacting case for $U = 4t$. The black circles mark the points used to patch the self-energy. Bottom row: cut of the occupation along the Brillouin zone paths reported as arrows in the insets. Blue dashed curves are results for the non-interacting system, while red dotted curves are for $U = 4t$.

feedback of other channels, that is, reducing the charge channel. The former effect dominates for small doping, the latter at large doping.

Trying to understand these self-energy feedback effects, we looked for possible changes in the Fermi surface shape by analyzing the momentum distribution

$$n^\Lambda(\mathbf{k}) = 2T \sum_{\nu} \frac{e^{i\nu 0^+}}{i\nu - \varepsilon_{\mathbf{k}} + \mu^\Lambda - \Lambda \Sigma^\Lambda(\mathbf{k}, \nu)}. \quad (33)$$

The factor 2 accounts for the spin degree of freedom. In Fig. 5 we show the non-interacting (top left) and interacting (top right) occupation in the first quadrant of the Brillouin zone for doping $x = 0.025$. The latter is computed at the critical scale Λ_c .

Comparing the two panels, one does not observe any relevant shift of the Fermi surface position, but the Fermi surface broadening is appreciably larger in the interacting case, due to the self-energy. Similar results apply for doping $x = 0.4$, as one can see from Fig. 6, where the broadening is more evident.

In Fig. 8, we compare the critical scales for dynamic (frequency dependent) and static (frequency independent) vertex, both without self-energy feedback. The static approximation is obtained by neglecting the frequency structures of the channels, and approximating

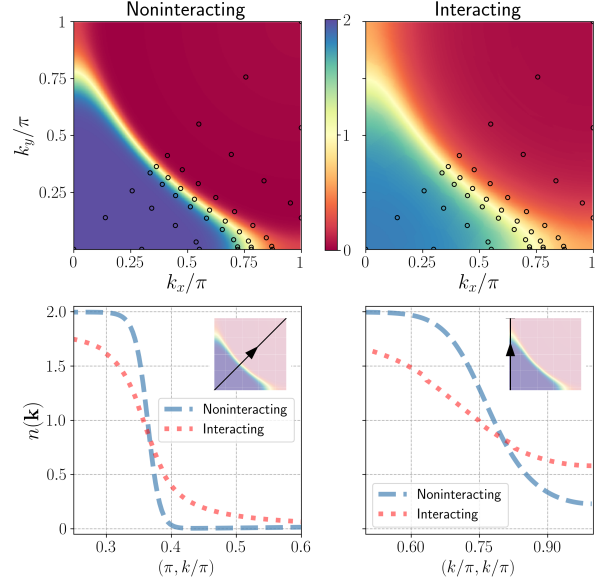


Figure 6. Top row: momentum distribution for $t' = -0.32t$, $T = 0.08t$ and doping $x = 0.4$. Left panel: non-interacting case. Right panel: interacting case for $U = 4t$. The black circles mark the points used to patch the self-energy. Bottom row: cut of the occupation along the Brillouin zone paths reported as arrows in the insets. Blue dashed curves are results for the non-interacting system, while red dotted curves are for $U = 4t$.

them with their value at a given choice of frequencies. Following Ref. 9, we evaluate the flow equations only for $\Omega = 0$, as transfer frequency, and $\pm\pi T$ as fermionic arguments. We observe that, the critical scale $1 - \Lambda$ is lower in the static case. This is due to two reasons, first, by taking $\nu_1 = -\nu_2 = \pi T$ the leading magnetic channel (at fixed bosonic frequency) is approximated by its lower value, as will be shown in the next paragraph. Second, in the static approximation the feedback of the other channels is overestimated, see below. For $x \geq 0.34$ according to our stopping criteria there is no divergence in any channel for the temperature considered.

In the same figure, the dashed green and the solid blue line denote the value of the maximum of the d -wave channel \mathcal{D}^Λ at Λ_c in the static and dynamic implementation, respectively. In both cases the d -wave is not the leading instability at the temperature under consideration,²⁵ but in the static case \mathcal{D}^{Λ_c} is orders of magnitude larger than in the dynamic case. This is effect of the vertex frequency dependence can be understood from Eqs. (A4) and (A6), where, neglecting the frequency structure, one does not take into account the decay of the magnetic channel for large (particle-hole) transfer frequencies.

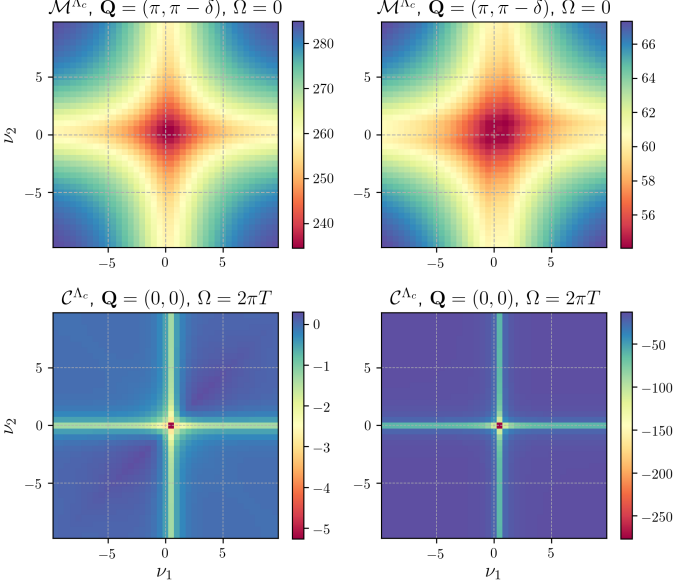


Figure 7. Frequency dependence of the magnetic (top) and charge (bottom) channel for $t' = -0.32$, $U = 4t$ and $T = 0.08t$. *Top left*: Magnetic channel $\mathcal{M}_{\mathbf{Q},\Omega}^{\Lambda}(\nu_1, \nu_2)$ with self-energy feedback at the instability vector and for vanishing frequency transfer, for doping $x = 0.025$. *Top right*: Magnetic channel $\mathcal{M}_{\mathbf{Q},\Omega}^{\Lambda}(\nu_1, \nu_2)$ without self-energy feedback at the instability vector and for vanishing frequency transfer, for doping $x = 0.4$. *Bottom left*: Frequency dependence of the charge channel $\mathcal{C}_{\mathbf{Q},\Omega}^{\Lambda}(\nu_1, \nu_2)$ with self-energy feedback at $\mathbf{Q} = (0, 0)$ and frequency transfer $\Omega = 2\pi T$, for doping $x = 0.025$. *Bottom right*: Frequency dependence of the charge channel $\mathcal{C}_{\mathbf{Q},\Omega}^{\Lambda}(\nu_1, \nu_2)$ without self-energy feedback at $\mathbf{Q} = (0, 0)$ and frequency transfer $\Omega = 2\pi T$, for doping $x = 0.4$.

B. Frequency dependence of vertex

We now discuss the remarkable frequency dependence of the vertex. In particular, we will look at the channels that show a divergence, that is, the charge and the magnetic instabilities observed in Fig. 2, while we refer to the Appendix for the pairing channels.

As mentioned in the previous section, the divergences of the charge and magnetic channels are quite different. The charge channel diverges for a finite frequency transfer, and only when we neglect the self-energy feedback. Since the dependence on the transfer momentum and frequency (\mathbf{Q}, Ω) has already been discussed in Ref. 12, we focus on the dependence on the fermionic frequencies. Therefore we present various color plots for fixed (\mathbf{Q}, Ω), showing the dependence on ν_1 and ν_2 .

In the top left panel of Fig. 7 we show the magnetic channel $\mathcal{M}_{\mathbf{Q},\Omega}^{\Lambda}(\nu_1, \nu_2)$ in the small doping region, where antiferromagnetism is the leading instability. The results shown have been calculated with self-energy feedback,

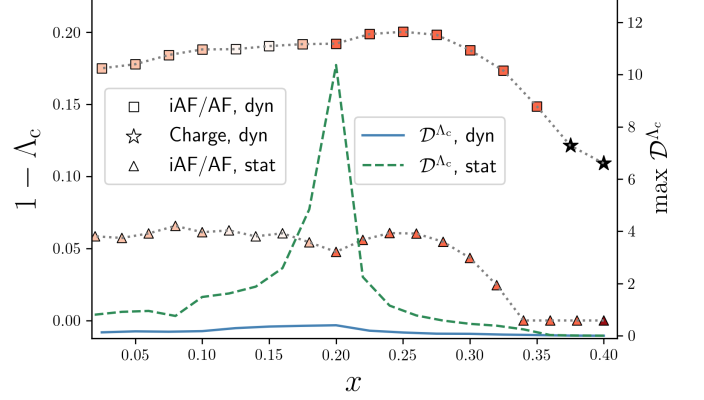


Figure 8. Critical scale $1 - \Lambda_c$ as a function of doping $x = 1 - n$, for $T = 0.08t$, $t' = -0.32t$ and $U = 4t$. Squares and triangles refer to leading couplings in the magnetic channel for frequency dependent (dynamic) and frequency independent (static) fRG. The black stars refer to a divergence in the charge channel at $\mathbf{Q} = (0, 0)$. For both fRG implementations, no self-energy feedback has been used. The color of squares and circles encodes the distance of the incommensurate magnetic \mathbf{Q} -vector from (π, π) : darker color corresponds to a larger distance, as in Fig. 2. The solid light blue (dashed green) line marks the maximal value of \mathcal{D}^{Λ} at the critical scale.

but the frequency structures we discuss do not depend strongly on the presence of the self-energy. For clarity we restrict the plots to the first 20 positive and negative Matsubara frequencies, larger frequencies can be deduced by the asymptotic behavior.¹⁴ When only one channel in Eq. (9) is taken into account, the fRG equations are equivalent to the RPA. The magnetic channel calculated with RPA would depend only on the frequency and momentum transfer, not on ν_1 and ν_2 . Hence any variation in the frequency structure has to be ascribed to the presence of the other channels in the fRG. The channel competition suppresses the magnetic channel: the largest value of \mathcal{M} is reduced compared to the RPA, and the frequency dependent structure at the center is further reduced compared to the asymptotic values at large ν_1, ν_2 .

In the bottom left panel of Fig. 7 we show the frequency dependence of the charge channel $\mathcal{C}_{\mathbf{Q},\Omega}^{\Lambda}(\nu_1, \nu_2)$ for a finite frequency transfer $\Omega = 2\pi T$, related to the charge instability discussed in Ref. 12 and above. The frequency structure is completely different from the magnetic channel. The charge channel assumes negative values, and the maximum is for frequencies $\nu_1 = \pi T$ and $\nu_2 = -\pi T$. This structure cannot be explained in terms of standard ladder diagrams. It might be related to the behavior of the retarded interaction described in Ref. 26.

In the two right panels of Fig. 7 we show the same quantities but for $x = 0.4$ and without self-energy feedback. In this case, the localized peak in the charge channel is the leading interaction. The position and shape of

the frequency structures are similar to the one described above.

C. Origin of charge singularity

To gain insight into the origin of the singular frequency structures observed in the charge channel, we identify a simple set of Feynman diagrams reproducing the same features. The main idea is that the magnetic channel, which is generated first, is responsible for the singular structure in the charge channel.

To check this qualitatively, we first compute an effective interaction by means of an RPA in the magnetic channel, and then insert this effective magnetic interaction into a subsequent RPA equation for the charge channel. Of course one does not expect quantitative agreement with the fRG, since we overestimate both interactions, but the approximation is sufficient to reproduce and explain the qualitative features we are interested in.

We start by introducing an effective interaction that includes the magnetic fluctuations as computed by RPA in the particle-hole crossed channel:

$$U_{\mathbf{Q},\Omega}^{\text{eff}} = \frac{U}{1 - U\Pi_{\mathbf{Q},\Omega}}. \quad (34)$$

Since the bare interaction U is local, U^{eff} depends only on the transfer momentum \mathbf{Q} and frequency Ω of the particle-hole bubble

$$\Pi_{\mathbf{Q},\Omega} = -T \sum_{\nu} \int_{\mathbf{p}} G_0(\mathbf{p}, \nu) G_0(\mathbf{p} + \mathbf{Q}, \nu + \Omega). \quad (35)$$

The magnetic effective interaction in Eq. (34) will now be used to compute the RPA equation for the charge channel. Adopting the simplified momentum dependences of the effective interactions used in the fRG calculation, only the momentum integrated, that is, local part of the magnetic interaction $U_{\Omega}^{\text{eff}} = \int_{\mathbf{Q}} U_{\mathbf{Q},\Omega}^{\text{eff}}$ contributes to the charge channel. We thus obtain $\tilde{C}_{\mathbf{Q},\Omega}(\nu_1, \nu_2) = \tilde{C}_{\mathbf{Q},\Omega}(\nu_1, \nu_2 - \Omega)$, where

$$\tilde{C}_{\mathbf{Q},\Omega}(\nu_1, \nu_3) = U_{\text{eff},\nu_1-\nu_3} [\delta_{\nu_1,\nu_3} + U_{\nu_1-\nu_3}^{\text{eff}} \Pi_{\mathbf{Q},\Omega}(\nu_1)]^{-1}, \quad (36)$$

with

$$\Pi_{\mathbf{Q},\Omega}(\nu) = - \int_{\mathbf{p}} G_0(\mathbf{p}, \nu) G_0(\mathbf{p} + \mathbf{Q}, \nu + \Omega). \quad (37)$$

Note that the fermion frequencies ν are not summed in $\Pi_{\mathbf{Q},\Omega}(\nu)$, and the inverse in Eq. (36) is a matrix inverse of the matrix with indices ν_1 and ν_3 . Eq. (36) is nothing more than an RPA equation with a frequency dependent interaction in the particle-hole channel.¹⁶ U^{eff} depends on $\nu_1 - \nu_3$ due to the frequency exchange from particle-hole crossed to particle-hole notation. In the case of a frequency independent effective interaction U_{eff} , Eq. (36) becomes ν_1 and ν_3 independent and only the summed

bubble $\Pi_{\mathbf{Q},\Omega}$ appears. The frequency dependence of U_{eff} qualitatively affects the results.

In Fig. 9, we show the charge channel as computed from Eq. (36) for $\mathbf{Q} = (0,0)$ and different Ω as a function of ν_1 and $\nu_2 = \nu_3 + \Omega$, for $T = t$ and $x = 0.375$. We have to choose such a high temperature to stay in a stable paramagnetic phase, due to the above-mentioned overestimation of the fluctuations within the RPA. In the more accurate fRG calculation the magnetic instability occurs at lower temperatures. The frequency structure in Fig. 9 for $\Omega = 2\pi T$ is very similar to the one shown in Fig. 7. The simple contributions considered here reproduce the position of the main structures, as well as the correct sign of the charge channel. This is true also for the other bosonic Matsubara frequencies shown here, for which we do not report the fRG results. Furthermore, upon lowering the temperature the charge channel diverges also for other finite bosonic Matsubara frequencies, while it does not diverge for $\Omega = 0$. From this we conclude that the frequency dependent effective magnetic interaction described above is responsible for the frequency structure of the charge channel observed in the fRG.

To understand why the divergence appears for a finite frequency Ω , we notice that in Eq. (36) the Ω dependence appears only through the bubble $\Pi_{\mathbf{Q},\Omega}(\nu)$. The frequency summed particle-hole bubble obeys the following relation:

$$\Pi_{\mathbf{Q} \rightarrow (0,0),\Omega} = T \sum_{\nu} \Pi_{\mathbf{Q} \rightarrow (0,0),\Omega}(\nu) = C \delta_{\Omega,0}, \quad (38)$$

where C is a positive constant that, at low temperature, approaches the density of states at the Fermi level. In the rightmost panel of Fig. 9, we show the bubble $\Pi_{\mathbf{Q}=(0,0),\Omega}(\nu)$ as a function of ν for different values of Ω . We note that it has a large negative peak for $\Omega = 2\pi T$. This is due to the property (38): the summed bubble must vanish for $\Omega \neq 0$, hence a large negative value is needed to cancel the positive contributions at large frequency. We have thus identified the origin of the frequency structure observed in the charge channel, which seems to be quite general and arises from simple Feynman diagrams.

Including the self-energy in the calculation of the bubble, Eq. (38) does not evaluate to a δ -function anymore, and the difference between the summed bubble at vanishing frequency and for frequency $2\pi T$ is diminished. This is probably the reason why the inclusion of the self-energy feedback prevents the unphysical divergence of the charge channel.

D. Self energy

We now discuss the frequency and momentum dependence of the self energy. In Fig. 10(a) we show the frequency dependence of the imaginary part of the self-energy at $T = 0.08t$ and low doping $x = 0.025$. The spread between the maximal and minimal self-energy at

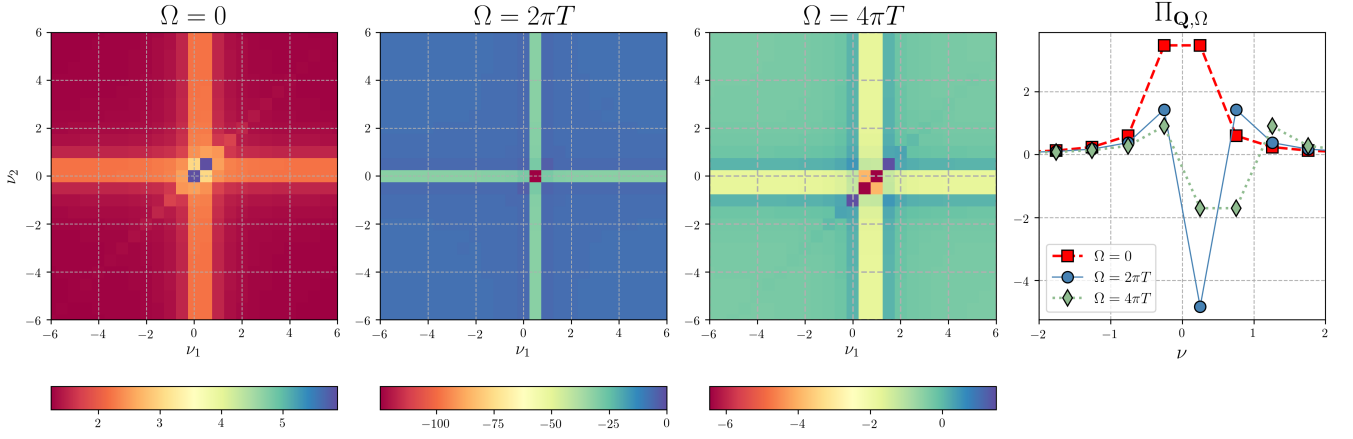


Figure 9. In the first three panels from the left, the charge channel $\mathcal{C}_{\mathbf{Q},\Omega}(\nu_1, \nu_2) = \tilde{\mathcal{C}}_{\mathbf{Q}=(0,0),\Omega}(\nu_1, \nu_2 - \Omega)$ computed from Eq. (36) is shown as a function of ν_1 and ν_2 for transfer frequencies $\Omega = 0$, $\Omega = 2\pi T$ and $\Omega = 4\pi T$, respectively. In the right panel, the bubble $\Pi_{\mathbf{Q}=(0,0),\Omega}(\nu)$ is shown as a function of ν for $\Omega = 0$, $\Omega = 2\pi T$ and $\Omega = 4\pi T$. The model parameters are $t' = -0.32$ and $U = 4$, the doping $x = 0.375$, and the temperature $T = t$.

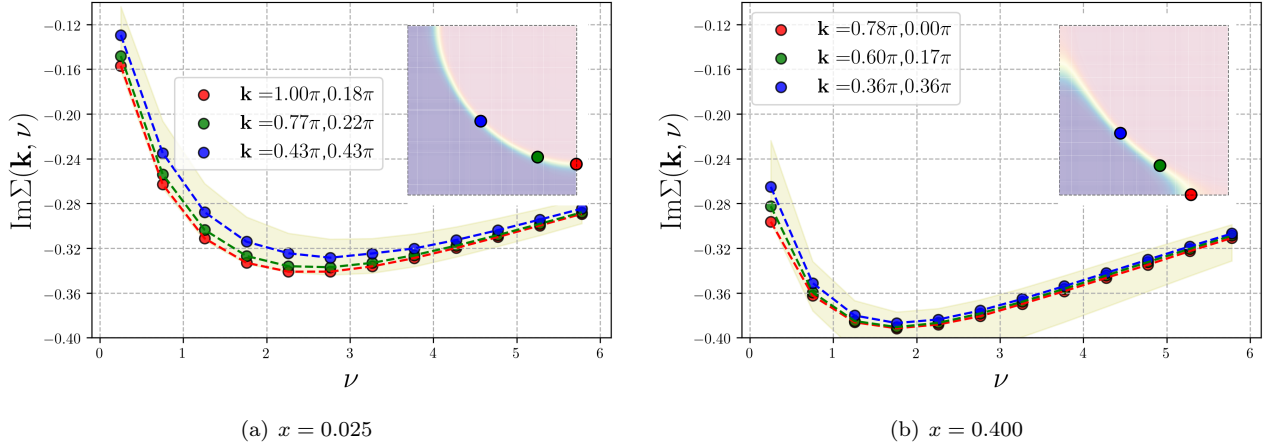


Figure 10. Self-energy as a function of frequency for $U = 4t$, $t' = -0.32t$ at temperature $T = 0.08t$. The location of the \mathbf{k} -point in the Brillouin zone is color coded in the inset. The position of all the patching points taken into account for the self-energy is shown as black circles in the top row of Figs. 5 and 6, and does not change during the flow. The shaded area highlights the region between the maximal and minimal value of the self-energy for each frequency.

each frequency is rather small, indicating that the self-energy did not develop a large momentum dependence even when the flow parameter reached the critical scale. For small frequencies, $|\text{Im}\Sigma(\mathbf{k}, \nu)|$ decreases as a function of decreasing frequency, for all momenta, as in a Fermi liquid. One would generally expect the antinodal region to be more affected by correlation effects. However, there is only a slight increase of $|\text{Im}\Sigma(\mathbf{k}, \nu)|$ in this region. At the temperature we are considering, we do not observe a tendency towards the opening of a momentum selective gap. In Fig. 10(b) we show the imaginary part of the self-energy for a larger doping $x = 0.4$. As in the previous case, we do not see much momentum differentiation.

The self-energy enters directly in the calculation of the momentum distribution through the Green's function, al-

ready discussed above, and shown in Figs. 5 and 6. In the bottom panels of these figures, we show how the momentum distribution evolves along two different cuts in the Brillouin zone, crossing the *nodal* and *antinodal* regions, respectively. The drop in the momentum distribution is sharper along the diagonal, and the self-energy effects are stronger along the antinodal cut. For doping $x = 0.4$ the broadening of the Fermi surface, already larger at the non interacting level, is further enhanced by the self-energy.

To study further the difference between nodal and antinodal regions in the iAF regime, we studied the quasi-particle weight²⁷ $Z_{\mathbf{k}}$, and the decay rate $\gamma_{\mathbf{k}}$. Instead of relying on analytical continuation, we have extracted the parameters directly from the imaginary axis data. To do so we have fitted the first few frequencies of the imagi-

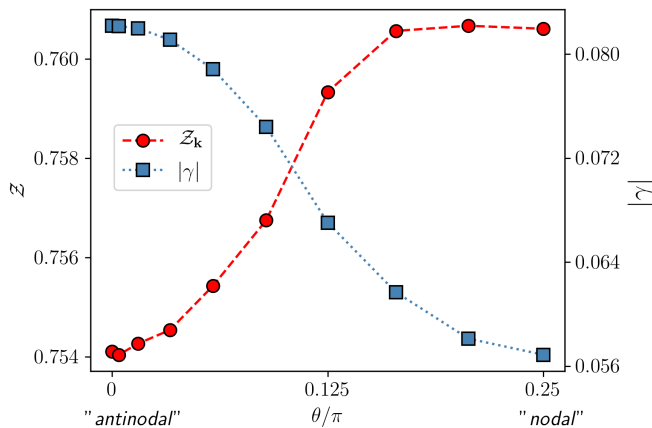


Figure 11. Quasiparticle weight Z_k and decay rate γ_k as function of the angle θ for the same parameters as in Fig. 10(a). The values on the left axis refer to the quasiparticle weight, the values on the right axis refer to the decay rate.

nary part of the self-energy with a polynomial of degree l : $\text{Im}\Sigma(\mathbf{k}, \nu) \approx a_0(\mathbf{k}) + a_1(\mathbf{k})\nu + \dots + a_l(\mathbf{k})\nu^l$ and we identified $\gamma_k = a_0(\mathbf{k})$ and $Z_k = [1 - a_1(\mathbf{k})]^{-1}$. The procedure only works if the temperature is small enough, and if the frequencies used for the fitting are not too high. We checked that the results were stable upon changing the number of frequencies and the order of the polynomial used for the fit. In Fig. 11 we plot Z_k and γ_k against the angle θ along the Fermi surface, $\theta = 0$ corresponding to the antinodal direction and $\theta = \pi/4$ to the nodal one. The variation of the quasiparticle weight along the Fermi surface is extremely small with Z_k assuming values between 0.754 and 0.760. On the other hand, the relative variation of the decay rate γ along the Fermi surface is sizable, varying from $\gamma \approx 0.056t$ to $\gamma \approx 0.082t$. These values are comparable with the temperature $T = 0.08t$.

Decay rates²⁸ and quasi-particle weights²⁹ were computed already in early fRG calculations from two-loop contributions to the self-energy, obtained by inserting the integrated one-loop equation for the vertex into the flow equation for the self-energy. In this way the computation of a frequency dependent vertex was avoided. The size and anisotropy of the decay rates obtained in these calculations are comparable to our results. The quasiparticle weight was even less reduced, and its anisotropy more pronounced, probably because the Fermi surface in Ref. 29 is more nested than ours and close to van Hove points.

We conclude that near the critical scale the system generically still has coherent quasiparticles along the Fermi surface, with a higher decay rate in the antinodal region. This is consistent with the observations of Ref. 30, where non-Fermi liquid behavior of the self-

energy was observed only very close to the critical temperature and in the immediate vicinity of the magnetic hot spots.

V. CONCLUSIONS

We have applied fRG flow equations to the two-dimensional Hubbard model, using a form factor decomposition for the momentum arguments of the two-particle vertex, but maintaining intact all the frequency dependences. To the best of our knowledge, this is the first time that such an approximation level has been achieved in a fRG calculation for interacting lattice fermions. Our results show that a complete treatment of the frequency dependence is not only possible, but also very important.

The complexity of the fully frequency dependent implementation is rewarded by the possibility of accessing and understanding the frequency structures arising in the flow. We confirm that, in a flow without self-energy feedback, there exist regions of parameter space where the vertex shows a divergence in the charge channel, as already found in Ref. 12. We are able to identify a simple set of Feynman diagrams that give rise to the above-mentioned divergence, that are likely to generate unexpected singular features in the charge channel also in other theories that take into account both the frequency dependence of the vertex and the interplay of different fluctuation channels.²⁶

The proper treatment of the frequency dependence of the vertex allows for a calculation of the frequency dependent self-energy. We observed that the feedback of the self-energy into the vertex flow plays an important role, also at the qualitative level, since it suppresses the divergence in the charge channel.

Given the increasing importance of the frequency dependence as more correlated regimes are approached, our work paves the way for future developments of the fRG for correlated fermion systems. At moderate coupling, like the one treated here, the combination of a frequency dependent vertex and self-energy feedback allows to revisit and improve previous results. At strong coupling, a non-perturbative starting point is needed. This is what is proposed in DMF²RG,⁴ where the flow starts from the DMFT solution for the vertex and the self-energy, which are both strongly frequency dependent. Therefore, consistently taking into account the frequency dependence is crucial to access strongly interacting fermion systems.

ACKNOWLEDGMENTS

We are grateful to M. Salmhofer, A. Eberlein, S. Andergassen, A. Toschi for useful discussion. We thank O. Gunnarsson for a critical reading of the manuscript and D. T. Mantadakis for comments and suggestions.

Appendix A: Flow equations

Here we present the final expressions for the flow equations in the pairing and in the charge channels. The flow equations for the magnetic channel have been presented in Sec. III.

The flow equation for the s -wave pairing channel reads

$$\dot{S}_{\mathbf{Q},\Omega}(\nu_1, \nu_3) = \frac{1}{2} \sum_{\nu} L_{\mathbf{Q},\Omega}^{s,\Lambda}(\nu_1, \nu) P_{\mathbf{Q},\Omega}^{s,\Lambda}(\nu) L_{\mathbf{Q},\Omega}^{s,\Lambda}(\nu, \Omega - \nu_3) + \frac{1}{2} \sum_{\nu} L_{\mathbf{Q},\Omega}^{s,\Lambda}(\Omega - \nu_1, \nu) P_{\mathbf{Q},\Omega}^{s,\Lambda}(\nu) L_{\mathbf{Q},\Omega}^{s,\Lambda}(\nu, \nu_3), \quad (\text{A1})$$

with

$$P_{\mathbf{Q},\Omega}^{s,\Lambda}(\omega) = \int_{\mathbf{p}} G^{\Lambda}(\mathbf{p}, \omega) S^{\Lambda}(\mathbf{Q} - \mathbf{p}, \Omega - \omega) + G^{\Lambda}(\mathbf{Q} - \mathbf{p}, \Omega - \omega) S^{\Lambda}(\mathbf{p}, \omega), \quad (\text{A2})$$

and

$$L_{\mathbf{Q},\Omega}^{s,\Lambda}(\nu_1, \nu_3) = U - S_{\mathbf{Q},\Omega}^{\Lambda}(\nu_1, \nu_3) + \int_{\mathbf{p}} \left[\mathcal{M}_{\mathbf{p},\nu_3-\nu_1}^{\Lambda}(\nu_1, \Omega - \nu_1) + \frac{1}{2} \mathcal{M}_{\mathbf{p},\Omega-\nu_1-\nu_3}^{\Lambda}(\nu_1, \Omega - \nu_1) - \frac{1}{2} \mathcal{C}_{\mathbf{p},\Omega-\nu_1-\nu_3}^{\Lambda}(\nu_1, \Omega - \nu_1) \right]. \quad (\text{A3})$$

The flow equation for the d -wave pairing channel reads

$$\dot{\mathcal{D}}_{\mathbf{Q},\Omega}^{\Lambda}(\nu_1, \nu_3) = \frac{1}{2} \sum_{\nu} L_{\mathbf{Q},\Omega}^{d,\Lambda}(\nu_1, \nu) P_{\mathbf{Q},\Omega}^{d,\Lambda}(\nu) L_{\mathbf{Q},\Omega}^{d,\Lambda}(\nu, \Omega - \nu_3) + \frac{1}{2} \sum_{\nu} L_{\mathbf{Q},\Omega}^{d,\Lambda}(\Omega - \nu_1, \nu) P_{\mathbf{Q},\Omega}^{d,\Lambda}(\nu) L_{\mathbf{Q},\Omega}^{d,\Lambda}(\nu, \nu_3), \quad (\text{A4})$$

with

$$P_{\mathbf{Q},\Omega}^{d,\Lambda}(\omega) = \int_{\mathbf{p}} [f_d(\mathbf{Q}/2 - \mathbf{p})]^2 \left[G^{\Lambda}(\mathbf{p}, \omega) S^{\Lambda}(\mathbf{Q} - \mathbf{p}, \Omega - \omega) + G^{\Lambda}(\mathbf{Q} - \mathbf{p}, \Omega - \omega) S^{\Lambda}(\mathbf{p}, \omega) \right], \quad (\text{A5})$$

and

$$L_{\mathbf{Q},\Omega}^{d,\Lambda}(\nu_1, \nu_3) = -\mathcal{D}_{\mathbf{Q},\Omega}^{\Lambda}(\nu_1, \nu_3) + \frac{1}{2} \int_{\mathbf{p}} (\cos p_x + \cos p_y) \left[\mathcal{M}_{\mathbf{p},\nu_3-\nu_1}^{\Lambda}(\nu_1, \Omega - \nu_1) + \frac{1}{2} \mathcal{M}_{\mathbf{p},\Omega-\nu_1-\nu_3}^{\Lambda}(\nu_1, \Omega - \nu_1) - \frac{1}{2} \mathcal{C}_{\mathbf{p},\Omega-\nu_1-\nu_3}^{\Lambda}(\nu_1, \Omega - \nu_1) \right]. \quad (\text{A6})$$

Since \mathcal{D} is generated exclusively by fluctuation contributions (not by the bare U), see Eq. (A6), it is the most sensitive channel to approximations on the frequency dependence. Neglecting the frequency dependence of the vertex one likely overestimates L^d , as already mentioned in Ref. 12.

The flow equation for the charge channel reads

$$\dot{C}_{\mathbf{Q},\Omega}^{\Lambda}(\nu_1, \nu_2) = \sum_{\nu} L_{\mathbf{Q},\Omega}^{c,\Lambda}(\nu_1, \nu) P_{\mathbf{Q},\Omega}^{\Lambda}(\nu) L_{\mathbf{Q},\Omega}^{c,\Lambda}(\nu, \nu_2 - \Omega), \quad (\text{A7})$$

with $P_{\mathbf{Q},\Omega}^{\Lambda}(\omega)$ as in Eq. (31), and

$$\begin{aligned} L_{\mathbf{Q},\Omega}^{c,\Lambda}(\nu_1, \nu_2) = & U - \mathcal{C}_{\mathbf{Q},\Omega}^{\Lambda}(\nu_1, \nu_2) + \int_{\mathbf{p}} \left[-2\mathcal{S}_{\mathbf{p},\nu_1+\nu_2}^{\Lambda}(\nu_1, \nu_2 - \Omega) + \mathcal{S}_{\mathbf{p},\nu_1+\nu_2}^{\Lambda}(\nu_1, \Omega + \nu_1) \right. \\ & + [\cos(Q_x) + \cos(Q_y)] \left(\mathcal{D}_{\mathbf{p},\nu_1+\nu_2}^{\Lambda}(\nu_1, \nu_2 - \Omega) - \frac{1}{2} \mathcal{D}_{\mathbf{p},\nu_1+\nu_2}^{\Lambda}(\nu_1, \Omega + \nu_1) \right) \\ & \left. + \frac{3}{2} \mathcal{M}_{\mathbf{p},\nu_2-\nu_1-\Omega}^{\Lambda}(\nu_1, \nu_2) + \frac{1}{2} \mathcal{C}_{\mathbf{p},\nu_2-\nu_1-\Omega}^{\Lambda}(\nu_1, \nu_2) \right]. \end{aligned} \quad (\text{A8})$$

The equation for the magnetic channel is reported in Eq. (30). The form factor decomposition allows to decouple the momentum integrals, in the calculation of the L 's, Eqs. (32), (A3), (A6) and (A8), from the frequency summations in the flow equations, hence reducing the numerical effort.

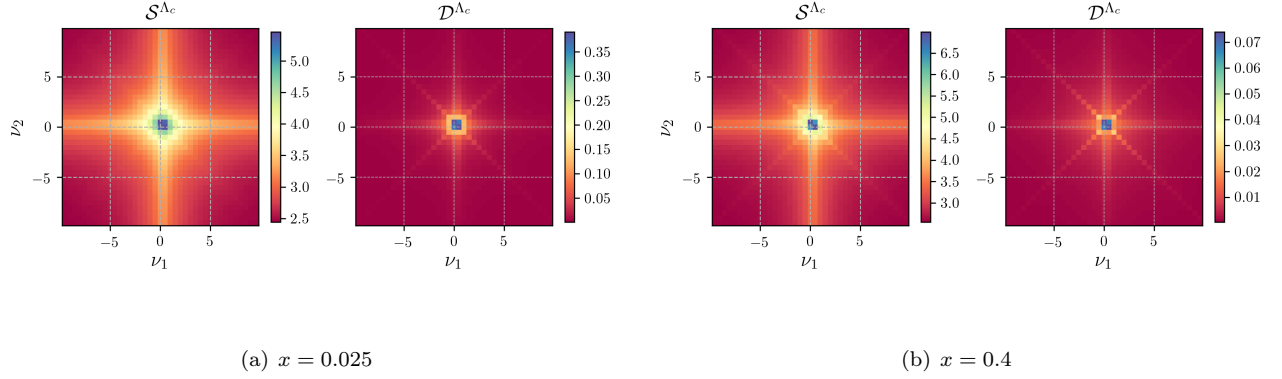


Figure 12. Frequency dependence of the pairing channels $\mathcal{S}_{\mathbf{Q},\Omega}^{\Lambda_c}(\nu_1, \nu_2)$ and $\mathcal{D}_{\mathbf{Q},\Omega}^{\Lambda_c}(\nu_1, \nu_2)$ for $\mathbf{Q} = (0,0)$ and $\Omega = 0$. The doping is $x = 0.025$ (left) and $x = 0.4$ (right). The other parameters are $T = 0.08t$, $t' = -0.32t$, and $U = 4t$.

Appendix B: Pairing channel

In Fig. 12 we display the frequency dependence of the pairing functions \mathcal{S} and \mathcal{D} for two distinct doping values $x = 0.025$ and $x = 0.4$. As a consequence of Eq. (A6), \mathcal{D}^{Λ_c} is decaying to zero in all directions for increasing $|\nu_1|, |\nu_2|$.¹⁴ The small numerical values of \mathcal{D}^{Λ_c} are due to three main reasons: first, the d -wave pairing is expected to increase suddenly only for temperatures very close to its critical temperature. Second, as argued in Ref. 12, previous fRG calculations with a static vertex overestimate the d -wave channel by neglecting the frequency dependence in Eq. (A6). Finally, the interaction scheme itself has a tendency to suppress the d -wave pairing, since in the terms of Ref. 14, the diagrammatic contributions to \mathcal{D} can be classified as *rest function*.

-
- ¹ J. Berges, N. Tetradis, and C. Wetterich, Phys. Rep. **363**, 223 (2002).
 - ² W. Metzner, M. Salmhofer, C. Honerkamp, V. Meden, and K. Schönhammer, Rev. Mod. Phys. **84**, 299 (2012).
 - ³ C. Wetterich, Physics Letters B **301**, 90 (1993).
 - ⁴ C. Taranto, S. Andergassen, J. Bauer, K. Held, A. Katanin, W. Metzner, G. Rohringer, and A. Toschi, Phys. Rev. Lett. **112**, 196402 (2014).
 - ⁵ D. Zanchi and H. J. Schulz, Zeitschrift für Physik B Condensed Matter **103**, 339 (1996).
 - ⁶ C. J. Halboth and W. Metzner, Phys. Rev. Lett. **85**, 5162 (2000).
 - ⁷ C. J. Halboth and W. Metzner, Phys. Rev. B **61**, 7364 (2000).
 - ⁸ C. Honerkamp, M. Salmhofer, N. Furukawa, and T. M. Rice, Phys. Rev. B **63**, 035109 (2001).
 - ⁹ C. Husemann and M. Salmhofer, Phys. Rev. B **79**, 195125 (2009).
 - ¹⁰ A. Eberlein and W. Metzner, Phys. Rev. B **87**, 174523 (2013).
 - ¹¹ H. Yamase, A. Eberlein, and W. Metzner, Phys. Rev. Lett. **116**, 096402 (2016).
 - ¹² C. Husemann, K.-U. Giering, and M. Salmhofer, Phys. Rev. B **85**, 075121 (2012).
 - ¹³ M. Kinza, J. Ortloff, J. Bauer, and C. Honerkamp, Phys. Rev. B **87**, 035111 (2013).
 - ¹⁴ N. Wentzell, G. Li, A. Tagliavini, C. Taranto, G. Rohringer, K. Held, A. Toschi, and S. Andergassen, ArXiv e-prints (2016).
 - ¹⁵ A. Georges, G. Kotliar, W. Krauth, and M. J. Rozenberg, Rev. Mod. Phys. **68**, 13 (1996).
 - ¹⁶ G. Rohringer, A. Valli, and A. Toschi, Phys. Rev. B **86**, 125114 (2012).
 - ¹⁷ G. Rohringer, H. Hafermann, A. Toschi, A. A. Katanin, A. E. Antipov, M. I. Katsnelson, A. I. Lichtenstein, A. N. Rubtsov, and K. Held, ArXiv e-prints (2017), arXiv:1705.00024 [cond-mat.str-el].
 - ¹⁸ A. Montorsi, *The Hubbard Model: A Reprint Volume* (World Scientific, 1992).
 - ¹⁹ C. Platt, W. Hanke, and R. Thomale, Advances in Physics **62**, 453 (2013).
 - ²⁰ M. Salmhofer and C. Honerkamp, Prog. Theor. Phys. **105**, 1 (2001).
 - ²¹ F. B. Kugler and J. von Delft, ArXiv e-prints (2017), arXiv:1703.06505 [cond-mat.str-el].
 - ²² The equation for the particle-particle channel is slightly different from the one usually reported in fRG, see, e.g., Ref. 9. This is because we took $V^\Lambda = V_{\uparrow\downarrow\uparrow\downarrow}^\Lambda$ instead of $V^\Lambda = V_{\uparrow\downarrow\downarrow\uparrow}^\Lambda$.
 - ²³ C. Honerkamp, D. Rohe, S. Andergassen, and T. Enss,

- Phys. Rev. B **70**, 235115 (2004).
- ²⁴ N. D. Mermin and H. Wagner, Phys. Rev. Lett. **17**, 1133 (1966).
- ²⁵ In the static case we observed d -wave instability for $T = 0.02t$.
- ²⁶ E. A. Stepanov, E. G. C. P. van Loon, A. A. Katanin, A. I. Lichtenstein, M. I. Katsnelson, and A. N. Rubtsov, Phys. Rev. B **93**, 045107 (2016).
- ²⁷ A. Abrikosov, L. Gorkov, and D. I.E., *Methods of quantum field theory in statistical physics* (Dover Publications, Inc., 1963).
- ²⁸ Honerkamp, C., Eur. Phys. J. B **21**, 81 (2001).
- ²⁹ C. Honerkamp and M. Salmhofer, Phys. Rev. B **67**, 174504 (2003).
- ³⁰ D. Rohe and W. Metzner, Phys. Rev. B **71**, 115116 (2005).